Since January 2020 Elsevier has created a COVID-19 resource centre with free information in English and Mandarin on the novel coronavirus COVID-19. The COVID-19 resource centre is hosted on Elsevier Connect, the company's public news and information website.

Sensors & Actuators: B. Chemical 359 (2022) 131591

Contents lists available at ScienceDirect

Sensors and Actuators: B. Chemical

journal homepage: www.elsevier.com/locate/snb

Controlled, partially exfoliated, self-supported functionalized flexible graphitic carbon foil for ultrasensitive detection of SARS-CoV-2 spike protein

Muhammad Adeel [a,b,*], Kanwal Asif [a,b], Vincenzo Canzonieri [b,c], Hasi Rani Barai [d], Md. Mahbubur Rahman [e,**], Salvatore Daniele [a,**], Flavio Rizzolio [a,b]

[a] Department of Molecular Sciences and Nanosystems, Ca'Foscari University of Venice, 30123 Venezia, Italy
[b] Pathology Unit, Centro di Riferimento Oncologico di Aviano (CRO) IRCCS, 33081 Aviano, Italy
[c] Department of Medical, Surgical and Health Sciences, University of Trieste, 34127 Trieste, Italy
[d] Department of Mechanical Engineering, Yeungnam University, Gyeongsan 38541, South Korea
[e] Department of Applied Chemistry, Konkuk University, Chungju 27478, South Korea

ARTICLE INFO

Keywords:
Self-supported electrode
Mild-oxidation
Functionalized flexible graphite foil
Immunosensors
COVID-19

ABSTRACT

This paper reports on an ultrasensitive and label-free electrochemical immunosensor for monitoring the SARS-CoV-2 spike protein (SARS-CoV-2 SP). A self-supported electrode, which can simultaneously serve as an antibody immobilization matrix and electron transport channel, was initially fabricated by a controlled partial exfoliation of a flexible graphitic carbon foil (GCF). Mild acidic treatment enabled the partial oxidation and exfoliation (down to a few layers) of the flexible GCF; this also provided a high percentage of oxygen functionality and an enhanced surface roughness. The substrate electrode was further functionalized with ethylenediamine (EDA) to provide a suitable platform with even a higher surface roughness, for the covalent immobilization of an anti-SARS-CoV-2 antibody. The change in the current response for the $[Fe(CN)_6]^{3-/4-}$ redox couple, induced by the binding of SARS-CoV-2 SP to the antibody immobilized on the electrode surface, was used to determine the SARS-CoV-2 SP concentration. The immunosensor thus prepared could detect SARS-CoV-2 SP within 30 min with high reproducibility and specificity over a wide concentration range (0.2–100 ng/mL). Detection limits of 25 pg/mL and 27 pg/mL were found in a phosphate buffer solution (pH 7.4), and diluted blood plasma, respectively. The immunosensor was also employed to detect SARS-CoV-2 SP in artificial human saliva.

1. Introduction

Since it was first discovered in December 2019 [1,2], the enduring outbreak of severe acute respiratory syndrome coronavirus 2 (SARS-CoV-2), or coronavirus disease-19 (COVID-19), has been challenging the global human health and economy and has caused colossal dysfunction of various activities. The mode of the virus transmission includes droplet, contact, airborne, fomite, and blood borne transmissions, which exacerbate the rapid spread of the virus [3,4]. Asymptomatic COVID-19 patients, without showing any signs or mild symptoms, are the major spreaders of this virus [5]. As of November 1, 2021, more than 247 million cases of COVID-19 have been identified around the globe, resulting in 5016,975 deaths [6]. Considering the limitations of availability, production, and the cost of the WHO-approved vaccines, the possible solution to control this lethal disease is still social distancing and the use of masks. However, the best solution to the problem is the isolation of the infected patients by earlier detection of COVID-19.

Currently, real-time reverse transcription-polymerase chain reaction (RT-PCR) is the primary method for diagnosis of SARS-CoV-2 infection. It is time-consuming, costly, and requires trained personnel. The highly contagious nature and the faster transmission rate of SARS-CoV-2 than SARS-CoV and Middle East respiratory syndrome can infect physicians and technical staff during the sample collection and analyses [5,7–9].

* Corresponding author at: Department of Molecular Sciences and Nanosystems, Ca'Foscari University of Venice, 30123 Venezia, Italy.
** Corresponding authors.
E-mail addresses: muhammad.adeel@unive.it (M. Adeel), mahbub1982@kku.ac.kr (Md.M. Rahman), sig@unive.it (S. Daniele).

https://doi.org/10.1016/j.snb.2022.131591
Received 15 November 2021; Received in revised form 11 February 2022; Accepted 15 February 2022
Available online 21 February 2022

Serological and immunological tests, principally based on the detection of antibodies developed in individuals upon exposure to the virus, are other reliable methods to diagnose COVID-19 [10–12]. Though rapid and highly specific, the latter methods are not suitable for the diagnosis at the early-stage of infection, since the detectable level of antibodies is produced after 10–14 days the onset of the symptoms [5,13]. For these reasons, antigen tests have received emergency authorization from FDA to diagnose SARS-CoV-2 [14]. Thus, there is still a crucial demand for sensitive and accurate diagnostic methods, and, possibly, portable devices that can directly detect virus antigens for the rapid diagnosis of SARS-CoV-2.

To date, a relatively few reports are available in the literature dealing with the detection of spike protein (SP) antigen for diagnosing SARS-CoV-2. They are based on optical methods (i.e., surface plasmon resonance and surface-enhanced Raman spectroscopy) [15], and a variety of electrochemical techniques [16–20] exploiting field-effect transistor systems [16,17], functionalized graphene [18]- and Au nanoparticles-modified electrodes [19], as well as Cu_2O nanocubes modified-screen printed-carbon electrodes [20].

Electrochemical-transduction-based devices have several advantages for biosensing and immunosensing, including point-of-care, point-of-need testing, and rapid measurements using small amounts or small volumes of samples. They are also characterised by high sensitivity, portability, and low-cost [21–23]. Moreover, electrochemical biosensors and immunosensors offer an excellent capability for the label-free detection of target analytes by exploiting even small changes in electrochemical signals that arise from redox indicators (e.g., $[Fe(CN)_6]^{3-/4-}$, $[Ru(NH_3)_6]^{3+}$, etc.), induced by the recognition events occurring on the electrode surface [24–26]. In this regard, the electrode modifiers and the electrode materials themselves play a crucial role both as biorecognition elements and for obtaining high sensitivity in the detection [27,28].

Among the electrode materials or modifiers, carbon-based materials (e.g., SWNT, graphene, graphitic carbon nitride) are attractive for developing biosensors and other electrochemical-based sensor systems [29–31]. This is mainly due to their low cost, non-toxicity, and ease of introducing functional groups. In particular, graphene and functionalized graphene materials have attracted significant interest for the specific tailoring of the electrode surfaces for detecting different biological compounds [32–34]. Typically, graphene and functionalized graphene are synthesized in powder form by mechanical and chemical exfoliation from pristine graphite. The surface of the starting materials is further modified by physical or chemical methods involving several steps [35–37], each of them requiring proper optimization. An easier way to obtain the desired characteristics and functionalization of an electrode surface is, for instance, to start from commercially available graphitic carbon foils (GCFs) and proceed by controlled partial exfoliation. The materials thus treated can act both as self-supported electrodes for the immobilization of recognition elements and electron transport channels.

In this work, we propose a new low-cost electrochemical sensor for the detection of SARS-CoV-2 SP. It is based on using controlled and partial oxidized GCFs (OGCFs), which are functionalized with ethylenediamine (EDA), by covalent bonding, using 1-Ethyl-3-(3-dimethlaminopropyl) carbodiimide (EDC) and N-hydroxysuccinimide (NHS) activators (designated as EDA-GCF). The anti-SARS-CoV-2 antibody is afterward immobilised on the EDA-GCF surface, where the SARS-CoV-2 SP antigen can bind with high affinity (Fig. 1). This provides a current change of the $[Fe(CN)_6]^{3-/4-}$ redox couple, which depends on the SARS-CoV-2 SP concentration. The performance of the proposed sensor is evaluated in phosphate buffer solution, diluted blood plasma and artificial human saliva samples.

2. Experimental section

2.1. Materials and reagents

Sulfuric acid (95–98%, H_2SO_4), nitric acid (63%, HNO_3), N-Hydroxysuccinimide (NHS), ($C_4H_5NO_3$), bovine serum albumins (≥

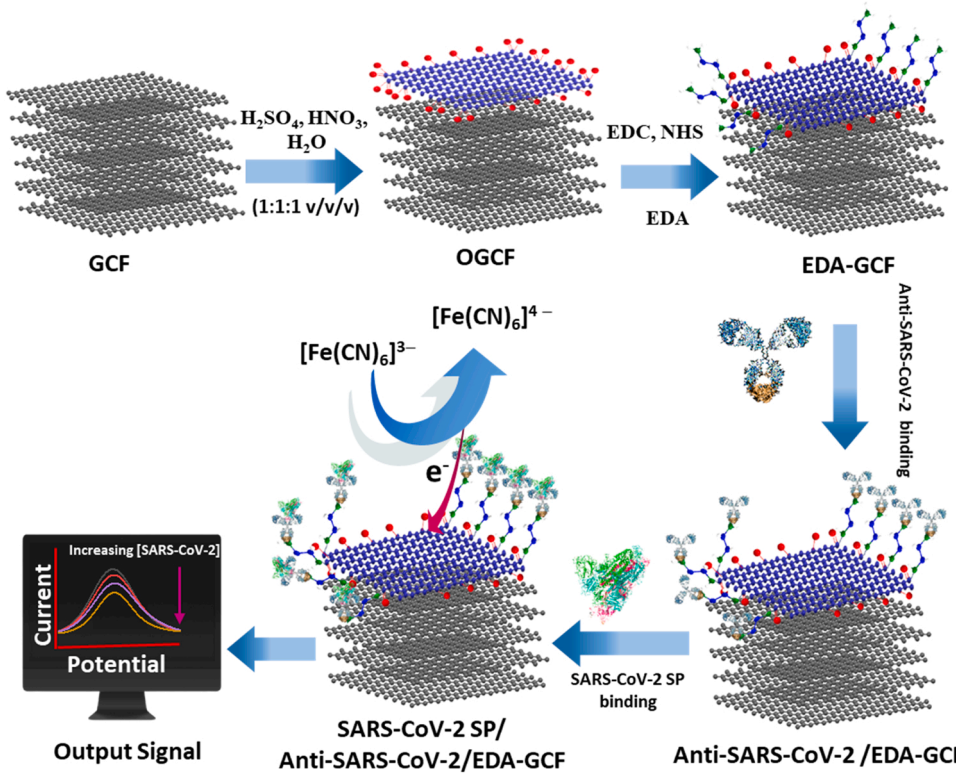

Fig. 1. Schematic illustration of the steps for the fabrication of the SARS-CoV-2 SP immunosensor: partial exfoliation and oxygen functionalization of GCF; EDA functionalization of OGCF; immobilization of anti-SARS-CoV-2; binding of SARS-CoV-2 SP; label-free detection of SARS-CoV-2 SP antigen using $[Fe(CN)_6]^{3-/4-}$.

98%, BSA), human serum albumins (≥ 98%, HSA), potassium hexacyanoferrate (II) (≥ 99%, $K_4[Fe(CN)_6]$), potassium hexacyanoferrate (III) (≥ 99%, $K_3[Fe(CN)_6]$), EDA (≥ 99%, $C_2H_8N_2$), blood plasma (BP) and saliva from human were purchased from Sigma Aldrich (St. Louis, MO, USA). Dulbecco's phosphate buffer solution (PBS, pH 7.4) without calcium and magnesium chloride and EDC were bought from Thermo Fisher Scientific (Waltham, Massachusetts, USA). Flexible GCF (99.8%) with a thickness of 0.35 mm was purchased from Goodfellow Cambridge (Huntingdon, UK). Recombinant monoclonal SARS-CoV-2 spike S1 antibody (anti-SARS-CoV-2) from Rabbit monoclonal antibody (MAb), SARS-CoV-2 SP, and SARS-CoV SP were purchased from Sino Biological (UK). Ultrapure water was prepared by a Milli-Q® IX water purification system (Sigma Aldrich). N_2 of high purity (> 99.99%) was provided by SIAD, Bergamo, Italy).

2.2. Apparatus and measurements

The morphology of the electrodes was examined by a field-emission scanning electron microscope (FE-SEM, Carl Zeiss Sigma VP). Elemental analyses were executed using energy-dispersive X-ray spectroscopy (EDS) (Quantax 200) associated with the FE-SEM. The crystallographic phase was analyzed by an X-ray diffractometer (Philips Xpert, Cu Kα radiation). The surface functional groups formed onto the GCF electrode after each chemical treatment (vide infra) were characterized by Fourier-transform infrared (FTIR) spectroscopy ((MIDAC, M4000). Raman spectra were measured using a Raman Spectrophotometer (Horiba Scientific, Xplora Plus, France) at room temperature with an excitation wavelength of 532 nm. The composition and the bonding nature of the sample were examined with an X-ray photoelectron spectroscopic system (XPS, Thermo Scientific™ K-Alpha, Thermo Fisher Scientific). The XPS spectra were fitted by Shirley type background correction followed by deconvolution using Gaussian (70%) and Lorentzian (30%) (GL30) fitting (Fityk software, version 1.3.1). The wetting behaviour of the samples was examined using a contact angle measurement system (CAM, SEO-300A, Korea). To this purpose, a drop of 5 μL of distilled water was placed on the surface and the contact angle was measured after 10 s. Each contact angle value refers to the average obtained from 5 drops.

A CHI920C workstation (CH Instruments, Texas-USA) was employed for both voltammetric and scanning electrochemical microscopy (SECM) measurements, and unless otherwise stated, they were performed in an electrochemical cell in a three-electrode configuration. Cyclic voltammetry (CV), differential pulse voltammetry (DPV) and chronoamperometry (CA) were performed using the modified/unmodified GCFs as the working electrodes, a Pt wire, and an Ag/AgCl (KCl, saturated) electrode were employed as counter and reference electrode, respectively. Fig. S1 shows the schematic representation of the electrochemical cell employed in CVs, DPVs and CA measurements. DPVs were acquired by using the following optimized parameters: pulse amplitude of 100 mV, pulse width of 2 ms, pulse period 1 s. In these measurements, an aqueous solution of $[Fe(CN)_6]^{3-/4-}$ (7 mM), containing 0.1 M KCl as supporting electrolyte, was employed. In SECM measurements, the electrochemical cell comprised a Pt microdisk 12.5 μm (nominal radius) electrode as the SECM tip, a Pt wire and an Ag/AgCl (KCl, saturated) electrode as counter and reference electrode, respectively. The Pt microelectrode was manufactured by sealing a platinum wire (Goodfellow Metals, Cambridge, UK) having 25 μm nominal diameter in a glass capillary tube following a standard procedure [38]. Afterward, it was tapered to a conical shape, polished with graded alumina powder (5, 1, and 0.3 μm), placed on a Buehler micro-cloth, and then characterized by CV at low scan rates and by SECM to evaluate the actual electrode radius of the microelectrode and the overall tip radius to the microdisk electrode radius ratio (*RG*) [13], respectively. The geometric radius of the microdisk was calibrated by recording the steady-state diffusion limiting current (I_o) from a 1 mM $Ru(NH_3)_6^{3+}$ solution containing 0.1 M KCl and using the following equation [39].

$$I_0 = 4\, n\, F\, D\, c^b\, a \quad (1)$$

where n is the number of electrons, F is the Faraday constant, D is the diffusion coefficient of the electroactive species (in this case 7.0×10^{-6} cm^2s^{-1}) [40], c^b is the bulk concentration and a is the radius of the microdisk. The *RG* parameter was evaluated by fitting experimental approach curves, recorded under purely diffusion-controlled conditions, to theoretical curves [41,42]. The *RG* thus estimated varied between 5 and 8. Unless otherwise stated, approach curves were plotted using normalized currents, I/I_0 (I is the current recorded at the tip to substrate distance, d), against normalized distance ($L = d/a$); normalised currents were also employed to construct the SECM images. They were acquired by using a 2 mM $[Fe(CN)_6]^{4-}$ solution containing 0.1 M KCl as a supporting electrolyte. Electrochemical impedance spectroscopy (EIS) was performed by using an impedance analyzer (IM6ex, Zahner-Elektrik GmbH & Co. KG). The measurements were acquired using the $[Fe(CN)_6]^{3-/4-}$ solution in the frequency range of 10^6 - 0.1 Hz, AC amplitude of 5 mV, and an applied potential of + 0.3 V.

2.3. Preparation of functionalized and exfoliated graphitic carbon foils

Prior to the exfoliation and functionalization steps, a series of GCFs (each 2 cm × 4 cm) was sequentially cleaned using an organic soap, deionized water, and ethanol under sonication; the GCFs were then dried with a stream of pure N_2. The OGCFs were prepared by placing the GCFs in a solution composed of H_2SO_4 (98%), HNO_3 (63%), and ultrapure water (1:1:1 v/v/v) at 70 °C for 24 h. Afterward, the samples were washed with ultrapure water several times with gentle shaking, dried under a stream of N_2, and then placed on a hot plate at 50 °C for 24 h. For the preparation of EDA-GCFs, the OGCFs were immersed in an EDC: NHS solution in PBS (pH 7.4) (EDC and NHS of 1 wt% corresponding to the weight of OGCF) and gently shaking for 5 h at room temperature. Afterward, the activated OGCFs were washed with ultrapure water several times and placed into an EDA solution (20 mL) at 80 °C for 24 h. Then, the samples were washed with ultrapure water under stirring to remove the unbound or physically adsorbed impurities and dried at 40 °C for 3 h. The as-prepared OGCF and EDA-GCF electrodes were stored at room temperature for further characterizations and applications.

2.4. Fabrication of the immunosensor

Anti-SARS-CoV-2 was covalently attached through an amide bond between the free $-NH_2$ functional groups of EDA-GCF and the $-COOH$ groups of anti-SARS-CoV-2 [18]. Briefly, EDA-GCF was placed in an electrochemical cell with a confined geometric area of 0.096 cm^2 defined by the O-ring (Fig. S1). Then, 400 μL of EDC (20 mM) and NHS (40 mM) solution in PBS (pH 7.4) was dropped onto the surface of EDA-GCF and kept for 5 h to activate the functional groups. Subsequently, the electrode was washed with PBS (pH 7.4), dried under a N_2 stream, and then 400 μL antibody (1 μg/mL in PBS pH 7.4) solution was dropped onto the activated EDA-GCF surface and incubated at 4 °C. Thereafter, the electrode was washed with PBS to remove the non-immobilized antibody. 1% BSA solution (400 μL) was dropped onto the anti-SARS-CoV-2/EDA-GCF electrode and kept for 1 h at 4 °C to block the unspecific. sites of the immunosensor. Finally, the anti-SARS-CoV-2/EDA-GCF immunosensor was used to bind SARS-CoV-2 SP spiked at different concentrations in the various investigated media. After each addition, the system was allowed to equilibrate for 30 min at 4 °C, then washed with PBS (pH 7.4) prior to the electrochemical analyses.

3. Results and Discussion

3.1. Electrode substrate characterization

The various electrodes were initially characterized by using spectroscopic, surface, and electrochemical techniques to ascertain the success of the various treatments, which ultimately led to a suitable substrate able to immobilize the anti-SARS-CoV-2 antibody. This system was afterward employed for the electrochemical detection of SARS-CoV-2 SP.

3.1.1. XRD, Raman, FTIR, and contact angle measurements

The degree of the exfoliation, oxidation, and functionalization of the GCF surface was investigated using X-ray diffraction (XRD) analyses. Fig. 2a shows the XRD patterns of the GCF, OGCF, and EDA-GCF. The GCF exhibited a high intensity typical sharp (002) peak of graphite at a 2θ angle of 26.10° with the interlayer spacing (d_{002}) of 3.41 Å [43,44]. Upon the oxidation of the GCF, a new low-intensity peak appeared at 2θ = 20.40°, attributed to the partial and fractional oxidation of the GCF surface only of a few layers [44]. The intercalation of oxygen atoms throughout the interlayer space, or in between the basal planes of the GCF, was excluded by the absence of the graphene oxide (GO) peak at about 10°, as instead was the case when GO was synthesized from graphite [44,45]. The above mentioned peak shifted to a higher 2θ angle (22.85°) in EDA-GCF, and this can be ascribed to the EDA attachment to the −COOH moieties as well as to the partial reduction of the surface oxygen functional groups of OGCF, induced by the EDA reducing agent [45,46]. The new low-intensity peak that appeared at 2θ = 11.35° in EDA-GCF was due to the intercalation of EDA throughout the interlayer space or in between the basal planes of GCF, as similarly observed for the intercalation of oxygen functionalities in between the basal planes of GO, prepared from graphite [44,45]. Furthermore, the high intense (002) peak was shifted to 26.45° for the EDA-GCF (Fig. 2b), suggesting the decrease of the interlayer spacing (d_{002} = 3.36 Å) [47]. This can be ascribed to the stitching of the GCF and OGCF layers by the EDA, induced by the covalent interaction and hydrogen bonding with the oxygen functional groups in GCF and OGCF at the edges and basal planes [48]. The full width at half maximum (FWHM) of the (002) plane for GCF was 0.39°, and was increased to 0.52° for EDA–GCF, indicating the reduction of the crystalline size of EDA-GCF (Fig. 2b) [47].

The compositions and the crystal structures of the GCF, OGCF, and EDA-GCF were examined further by Raman spectroscopy, and the

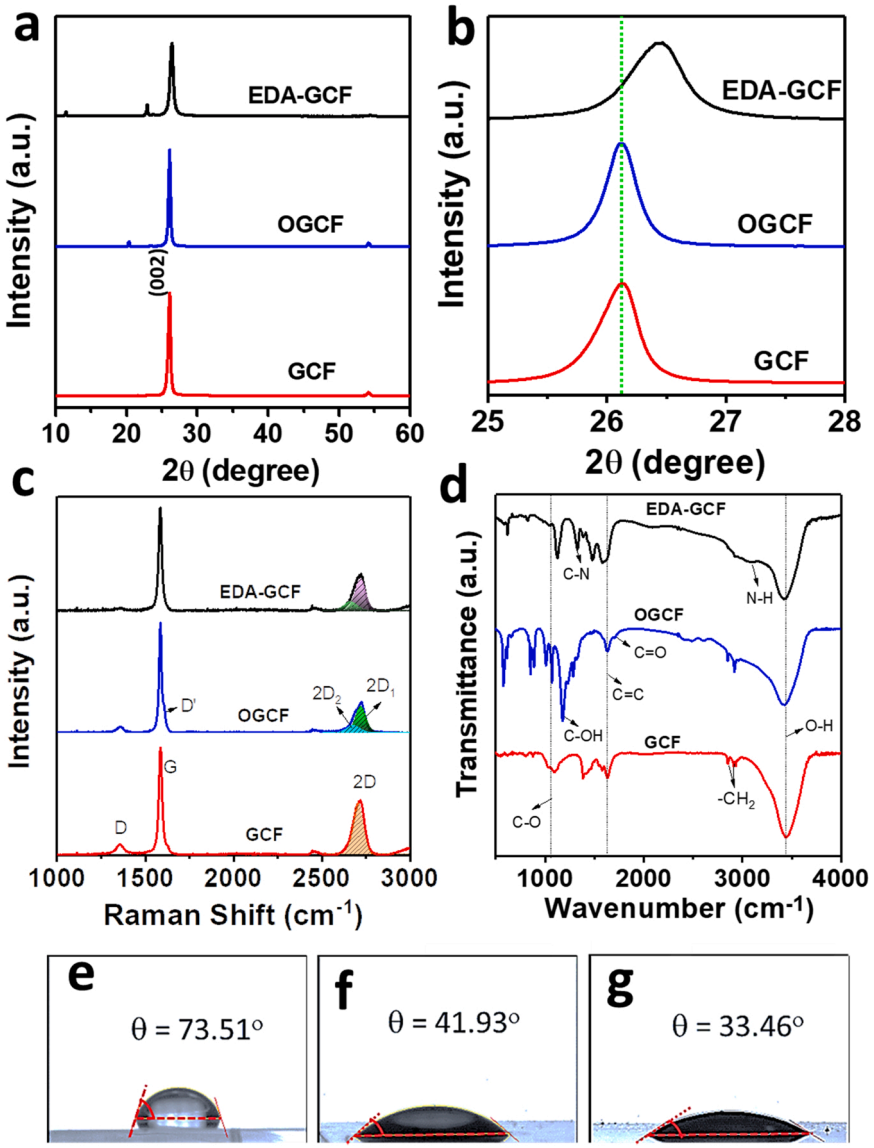

Fig. 2. (a) XRD pattern, (b) magnified XRD pattern, (c) Raman spectra, and (d) FTIR spectra of GCF, OGCF, and EDA-GCF. (e-g) contact angles of GCF, OGCF, and EDA-GCF, respectively, using ultrapure water.

resulting spectra are shown in Fig. 2c. All the samples displayed the characteristics G (1590 cm^{-1}), 2D (2715 cm^{-1}), and D (1350 cm^{-1}) bands without any noticeable shift of the peak positions [49]. However, both GCF and OGCF exhibited an additional D′ band (1615 cm^{-1}), indicating a disordered structure due to the presence in it of oxygen functional groups [49,50]. The intensity of this D′ band in OGCF was higher than that of GCF, suggesting that the oxidation process increased the disorder in the structure. Instead, after EDA functionalization and partial reduction of OGCF, the disorder and defects in the structure decreased. Additionally, both OGCF and EDA-GCF exhibited two 2D peak profiles ($2D_1$ and $2D_2$), indicating the formation of perfectly A-B stacked few layers GO like OGCF and EDA-GCF. In contrast, GCF showed a single peak profile with multilayer structures, which is consistent with the general characteristics of graphite [50]. However, the intensity of the 2D peak in OGCF decreased compared to that of the GCF. This could be due to the presence of defects and functional groups, which were increased in the EDA-GCF, suggesting the reduction of the defects by EDA functionalization and partial reduction of oxygen functionalities, consistent with the intensity profiles of D bands of the samples [49].

Fig. 2d shows the FTIR spectra of the samples. All the samples exhibited the common FTIR band of O–H stretching vibrations at 3534 cm^{-1}, due to the presence of adsorbed water molecules, the C═C stretching vibrations (1630 cm^{-1}), the $-CH_2$ stretching bands (2930 and 2845 cm^{-1}), and the C–O bands (1060 cm^{-1}) [45,48]. The OGCF displayed the additional C═O stretching band of the COOH groups at 1708 cm^{-1} and C–OH vibrations at 1170 cm^{-1}. The EDA-GCF showed the additional strong N − H stretching and bending vibrations at 3090 and 1580 cm^{-1}, respectively, and C–N vibrations at 1320 cm^{-1} together with the C═O stretching and C–OH vibrations at 1120 cm^{-1} [48]. These results further suggest the successful synthesis of OGCF and EDA-GCF. Nevertheless, the decrease of the C–O peak area and intensity in the EDA-GCF, compared to the OGCF, indicated the partial reduction of the OGCF induced by the EDA, which is consistent with the XRD observations.

Fig. 2e-g show the contact angle values and wetting behaviour of the electrodes, measured after 10 s the water drop was applied on the surfaces of the electrodes. It is apparent that the surface wettability of the GCF is increased somewhat, upon the oxidation and EDA functionalization. The decrease of the contact angle, passing from GCF (73.51°) to OGCF (41.93°), is conceivably due to the hydrogen bonding between the water molecules and the oxygen functionalities generated by the oxidation. The further decrease of the contact angle (33.46°), upon OGCF functionalization with EDA, supports the success of the reaction and intercalation of the molecule within the layers of OGCF.

3.1.2. Morphological characterization

Fig. 3a-f shows the FE-SEM images of the GCF, OGCF, and EDA-GCF surfaces. The GCF surface exhibited small wrinkles, while that of the OGCF was covered with partially exfoliated GO nanosheets. The EDA functionalization induced the decrease in the size of the nanosheets and an increase of the EDA-GCF surface roughness, compared to that of GCF. This was also evident from the corresponding digital photographic pictures and could also be observed by the naked eye (insets in Fig. 3b-f). The comparison of the EDS spectra of GCF (Fig. S2) and OGCF (Fig. S3), together with the EDS elemental mapping of oxygen and carbon in OGCF (Fig. S3), indicated the presence of a high-density of oxygen functionalities in OGCF, compared to that of GCF. The EDA functionalized-electrode surface examined by EDS revealed the presence of a high density and the homogeneous distribution of carbon, nitrogen, and oxygen (Fig. 3g-i, respectively; see also EDS spectra in Fig. S4), designating the successful functionalization with EDA.

The mechanism of exfoliation, oxidation, and EDA functionalization of the GCF is schematically shown in Fig. 3j. Upon the mild acidic treatment, the SO_4^{2-}, NO_3^-, and H^+ ions were easily intercalated into the GCF layers. This led to a much higher interlayer distance between the graphite sheets (0.334 nm), compared to the ionic radius (r) of H^+ (r_{H^+} = 0.037 nm), SO_4^{2-} ($r_{SO_4^{2-}}$ = 0.258 nm), and NO_3^- ($r_{NO_3^-}$ = 0.179 nm) [47]. This also favoured the formation of OGCF. The low hydrophilicity, the floating behaviour of the GCF and the absence of any forced convection (stirring, sonication, etc.), during preparation, enabled controlling the partial oxidation and exfoliation of the GCF surface, which occurred only in the zones of the material in direct contact with the acidic solution.

The increase of the hydrophilicity of the OGCF enabled the EDA functionalization through a covalent bond between the –COOH groups of OGCF and the $–NH_2$ groups of EDA; it was also favoured by the EDC and NHS activation. The spontaneously formed oxygen functionalities (–OH and –COOH) at the edges and basal planes of GCF also induced a chemical interaction (hydrogen bonding) with the intercalated small EDA molecules. Both of these interactions made it possible to stitch the GCF sheets across basal planes and edges (scheme in Fig. 3j). This view agrees with the FE-SEM image of EDA-GCF. Furthermore, bridging or stitching through basal planes between the adjacent GCF layers conceivably induced the decrease in the interlayer distance in EDA-GCF, as was evident from the XRD results.

3.1.3. XPS analysis

XPS was used to examine the elemental compositions and types of bonds that exist in the GCF, OGCF, and EDA-GCF. As anticipated, the XPS survey spectra of all the samples predominantly showed the presence of carbon and oxygen peaks, while EDA-GCF exhibited an additional nitrogen peak arising from the EDA functionalization (Fig. 4a). As is evident from data shown in Table S1, the oxidation process effectively increased the surface oxygen content from 14.33 at% of GCF to 30.84 and 22.88 at% for OGCF and EDA-GCF, respectively. On the other hand, the higher N (26.97 at%) content in EDA-GCF and the decrease of the O at%, with respect to OGCF, suggested the incorporation of EDA between the adjacent GCF layers, the partial reduction of OGCF, and the covalent attachment of EDA. The high-resolution XPS spectra of C 1 s and N 1 s were investigated to examine the types of chemical bonds and the vacancies or defects present in the sample structures. Fig. 4b shows the C 1 s spectra of the GCF, OGCF, and EDA-GCF. The high-resolution C 1 s XPS spectra for all the samples were fit into five component peaks. The peaks positioned at 284.80 eV for all the samples were ascribed to the delocalized C═C bonds, while the peaks located at 286.60 and 286.12 eV for GCF and OGCF, respectively, were attributed to the localized C-C bonds with the percentage of 40.44% and 39.55%, respectively [51]. The increase of the intensity of the peak at 286.30 eV of 46.75% for EDA-GCF was ascribed to the combination of localized C–C and C–N peaks [51,52]. Both GCF and OGCF exhibited –COOH peaks at 290.0 and 289.50 eV, respectively, with percentage of 2.10% and 6.20%, respectively, indicating the high degree of oxidation of GCF [52]. The intensity of the –COOH peak decreased in EDA-GCF, while a new peak appeared at lower binding energy (288.31 eV), due to the C═O bond originating from the amide bond [53]. All the samples exhibited the additional small peaks due to C–OH at 286.69 eV for GCF, at 286.15 eV for OGCF, and at 286.50 eV for EDA-GCF, together with the C atoms neighbouring lattice vacancies 5.28%, 8.6%, and 4.41%, respectively, for GCF, OGCF, and EDA-GCF at 284.0, 284.15, and 283.95 eV, respectively [52]. The variation of the degree of lattice vacancies is highly consistent with the Raman results. Furthermore, we analyzed the high-resolution N 1 s spectra of EDA-GCF as shown in Fig. 4c. They were fitted into three component peaks. The high-intensity peak located at 401.75 eV was assigned to the C–N bond, while the other low-intensity peaks located at 399.5 and 402.10 eV were ascribed to the $–NH_2$ and N–C═O bonds [52–54]. These data suggested the successful EDA functionalization.

3.1.4. Electrochemical measurements

The general electrochemical behavior of the GCF, OGCF, activated OGCF (Act. OGCF), and EDA-GCF electrodes was, preliminary,

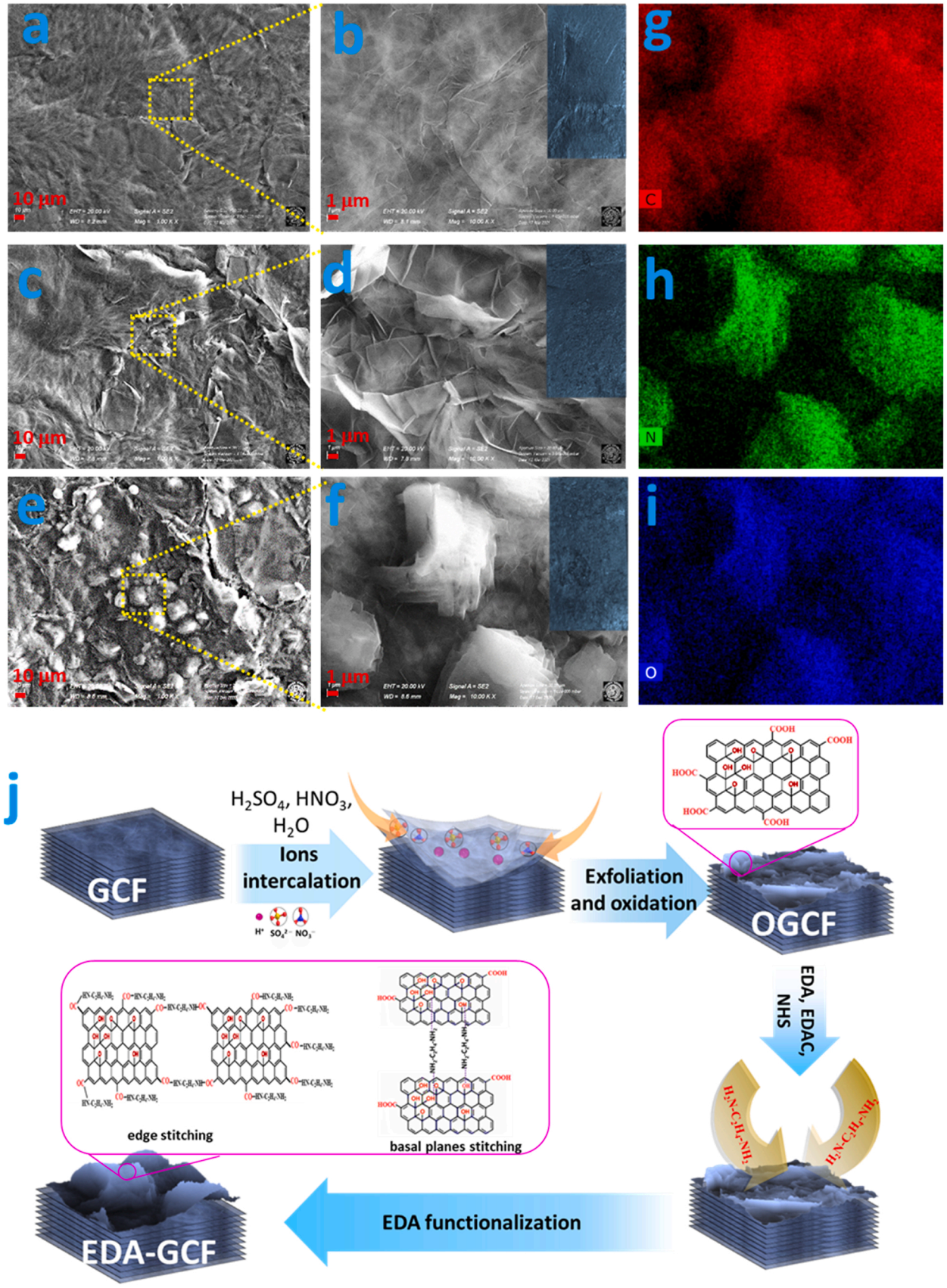

Fig. 3. FE-SEM images of (a-b) GCF, (c-d) OGCF, and (e-f) EDA-GCF (insets of b, d, and f show the digital photographic images of GCF, OGCF, and EDA-GCF, respectively). (g-i) EDS mapping of C, N, and O, respectively, in EDA-GCF. (j) Schematic of the mechanism of controlled partial exfoliation and the preparation of OGCF and EDA-GCF.

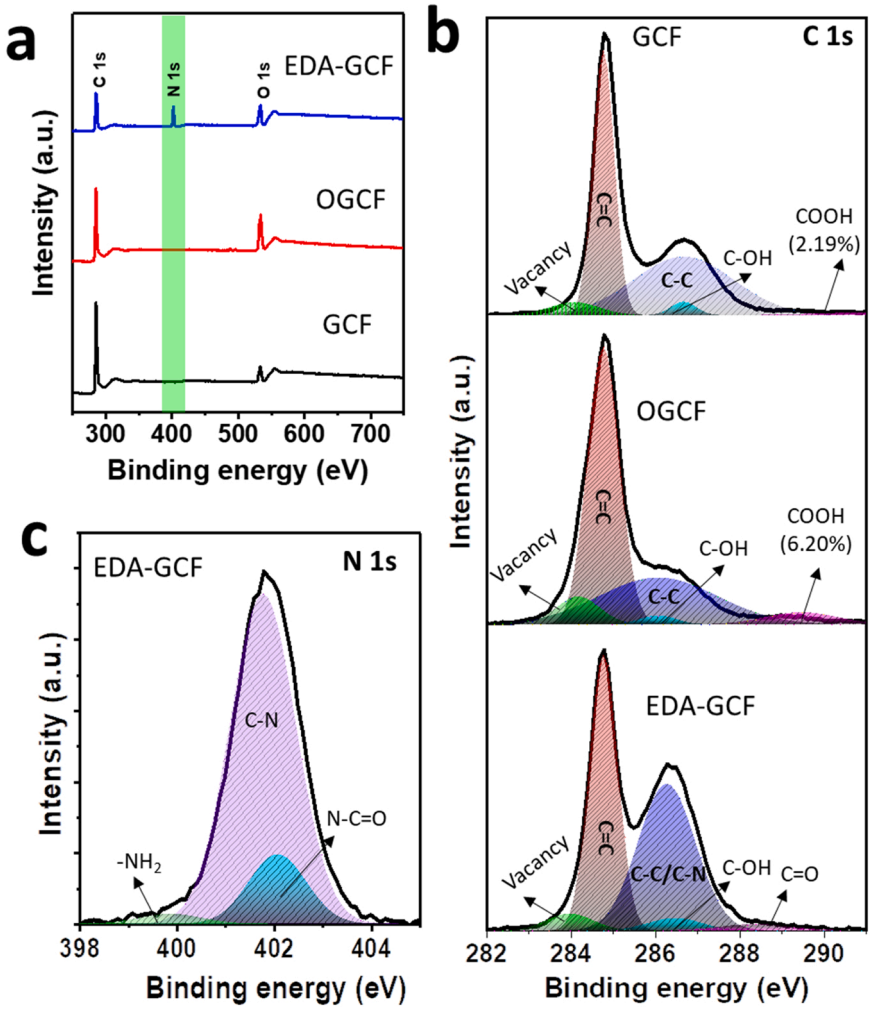

Fig. 4. (a) XPS survey spectra of the GCF, OGCF, and EDA-GCF. (b) High-resolution C 1 s spectra of GCF, OGCF, and EDA-GCF, and (c) N 1 s spectra of EDA-GCF. Solid lines and the shaded area indicate the experimental and fitted data, respectively.

characterized by CV (Fig. 5a,d), electrochemical impedance spectroscopy (EIS) (Fig. 5b), CA (Fig. 5e) and DPV (Fig. S5) using an aqueous solution of $[Fe(CN)_6]^{3-/4-}$ in phosphate buffer (PBS, pH 7.4). The inset in Fig. 5a summarizes the anodic peak current density (J_{pa}) and the peak-to-peak potential separation (ΔE_p) obtained from the CVs at 100 mV/s with the various electrodes. As is evident, the CV recorded at the GCF exhibits a redox pattern having a quite large ΔE_p (180 mV) and J_{pa} of 1.44 mA/cm^2. The apparent sluggish electron transfer process can be in part due to a local electrostatic repulsion between negatively charged carboxyl ions (COO^-), formed spontaneously on the GCF surface (see above), with the negatively charged $[Fe(CN)_6]^{3-/4-}$ redox couple [55]. A more drown out CV, having a somewhat larger ΔE_p (190 mV) and a smaller J_{pa} (1.41 mA/cm^2) was recorded at the OGCF. This can be attributed to the enhanced electrostatic repulsion between the high density of COO^-, present onto the OGCF surface, with the negatively charged $[Fe(CN)_6]^{3-/4-}$ redox probe [55,56], as schematically depicted in Fig. 5c. After the activation of the carboxylic groups, by using EDC and NHS, the Act. OGCF displayed a smaller ΔE_p (110 mV) and a higher J_{pa} (2.71 mA/cm^2). This can be ascribed to the neutralization of negatively charged COO^- in the OGCF surface by the small NHS molecules (Fig. 5c) [57]. The incorporation of EDA into the porous material led to a small decrease of J_{pa} (2.05 mA/cm^2), while ΔE_p remained essentially constant (110 mV). The information gathered from the CVs was confirmed by EIS measurements. In fact, as is evident from Fig. 5b, all the electrodes exhibit Nyquist type plots with the interfacial charge transfer resistance (R_{ct}) and Warburg diffusion resistance (Z_w) at the high and low-frequency region, respectively [58]. The variation of the R_{ct} for all the electrodes well agrees with the electrochemical features obtained from CVs. In particular, R_{ct} of 852.0, 1729.50, 158.0, and 240.25 Ω were found at the GCF, OGCF, Act. OGCF, and EDA-GCF electrodes, respectively.

Fig. 5d shows the CVs recorded at the EDA-GCF electrode in the $[Fe(CN)_6]^{3-/4-}$ solution at different scan rates. Both J_{pa} and cathodic peak current density (J_{pc}) increased with increasing scan rate, and they were proportional to the square root of the scan rates (inset of Fig. 5d). The linear regression analysis of experimental points provided the equations for J_{pa} (mA/cm^2) = 0.24 (± 0.0013) × $\nu^{1/2}$ (mV/s)$^{1/2}$ – 0.22 (± 0.007; R^2 = 0.999) and for J_{pc} (mA/cm^2) = −0.20 (± 0.002 × $\nu^{1/2}$ (mV/s)$^{1/2}$ + 0.11 (± 0.01; R^2 = 0.999). These results suggest the occurrence of a diffusion-controlled redox process [22]. Furthermore, the electrochemical stability of the EDA-GCF electrode was analyzed by repetitive CV scans (i.e., 100 cycles, Fig. 5e) and CA measurements for 1 h (inset of Fig. 5e). The CVs revealed a relative standard deviation (RSD) of only 2.10% (from four replicates) for the J_{pa}, while the quasi steady-state current density value in the CA was almost stable for 1 h. These characteristics hold promise for the development of stable electrochemical sensors based on EDA-GCF materials.

The electrochemical behavior of the various electrodes was also investigated by DPV, which was used for the analytical measurement (vide infra). Typical DPVs are shown in Fig. S5, from which it is evident that the trend of the peak current for the various electrodes is congruent with that obtained by CVs (Fig. 5a).

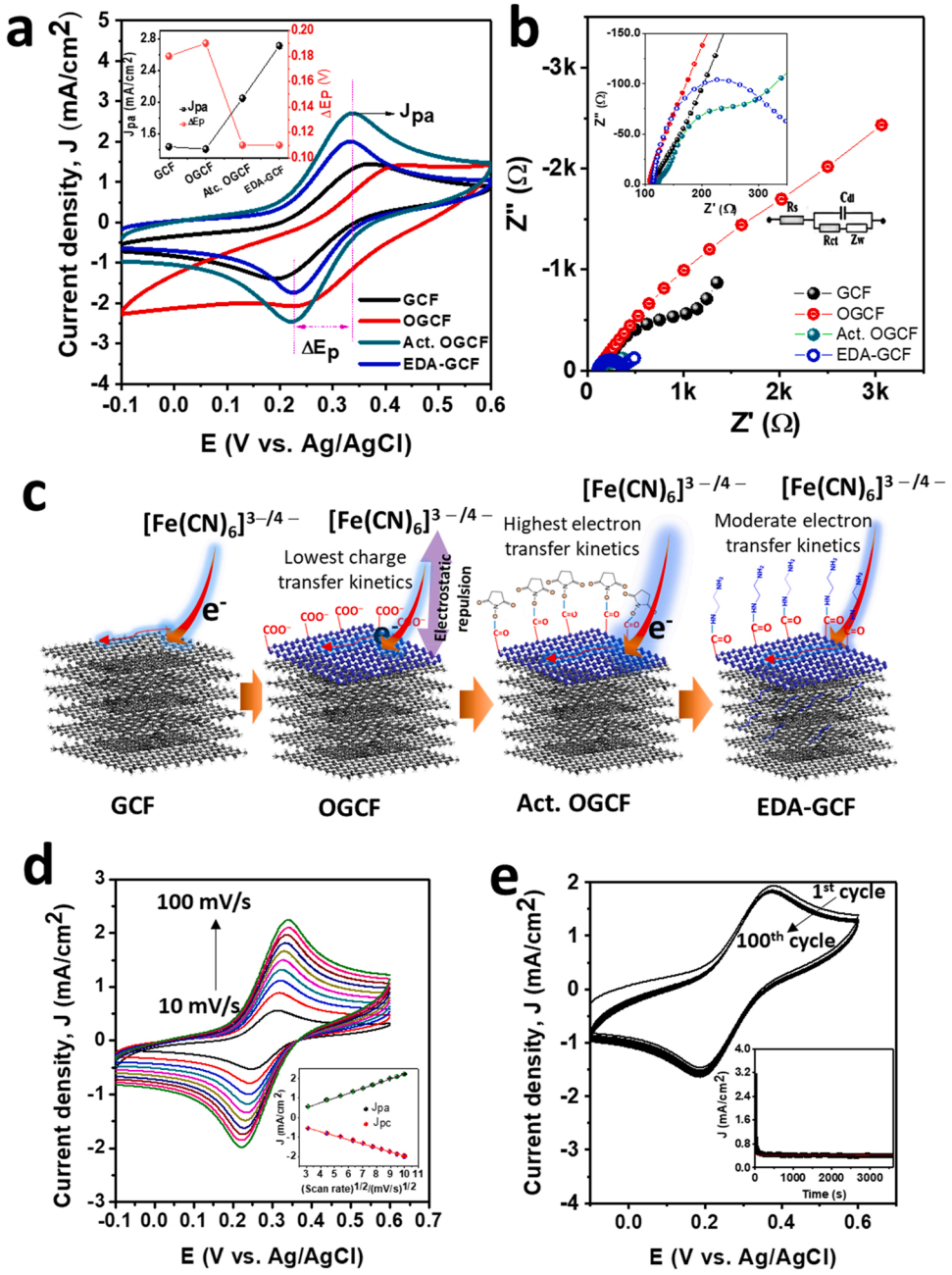

Fig. 5. (a) CVs (scan rate: 100 mV/s) (inset shows the plots of the summary of J_{pa} and ΔE_p) and (b) Nyquist plots (inset shows the magnified Nyquist plots) of GCF, OGCF, Act. OGCF, and EDA-GCF electrodes. (c) Schematic of the GCF modification and electron transport of the various electrodes. (d) CVs of EDA-GCF electrodes in $[Fe(CN)_6]^{3-/4-}$ redox electrolyte solution at different scan rates (10, 20, 30, 40, 50, 60, 70, 80, 90, and 100 mV/s) and (e) consecutive CVs (100 cycles) of the EDA-GCF electrodes in $[Fe(CN)_6]^{3-/4-}$ redox electrolyte solution at a scan rate of 100 mV/s (inset shows the CA plot of the EDA-GCF electrodes in $[Fe(CN)_6]^{3-/4-}$ redox electrolyte solution at 0.335 V).

3.1.5. *Scanning electrochemical microscopy (SECM) measurements*

To acquire information on conductivity and, more in general, on the electrochemical activity of the investigated surface materials (of bare, activated, and EDA-functionalized GCF) at micrometer spatial resolution, a series of SECM measurements was performed. These were carried out with the substrates being unbiased, thus allowing probing their surface status without any direct electrochemical perturbation. The SECM tip signal was originated from the one electron oxidation of $Fe(CN)_6^{4-}$ to $Fe(CN)_6^{3-}$, while keeping the potential of the microelectrode constant at 0.45 V, vs. the Ag/AgCl reference electrode. In these experiments, when the tip is positioned far above the substrate, the diffusion-limited current predicted by Eq. (1) [39] (see the experimental section) is recorded. When the microelectrode tip is brought closer to the investigated surface, the tip current is perturbed from its value in the bulk solution by the presence of the substrate, and two situations can occur. If the microelectrode tip approaches an insulating or low conducting/active region, the current decreases as the tip-to-substrate distance decreases, due to blockage of diffusion of the electroactive species towards the tip [59] (negative feedback). Instead when the microelectrode tip approaches a conducting/active region, the current increases with decreasing the tip-to-substrate distance, due to regeneration of the redox mediator at the substrate/solution interface (positive feedback, Fig. S6) [59]. Therefore, the analysis of the approach curves can provide useful information about the nature and reactivity of the investigated substrates. Fig. 6a shows typical approach curves obtained above the various substrates. It is evident that, in any case, positive feedback occurred. However, the normalized current, I/I_0 (although affected from tilting problems [59]), at close distances, followed the order: Act. OGCF > EDA-GCF > GCF, indicating a decreasing of the conductivity/activity (or smaller conductive/active regions) of the substrates in the same order. The local activity of the substrates was ascertained also by imaging a few hundred μm^2 of the surface area of the substrates by SECM. These experiments were performed by positioning the platinum micro-tip at about 20 μm above the substrate surface (by

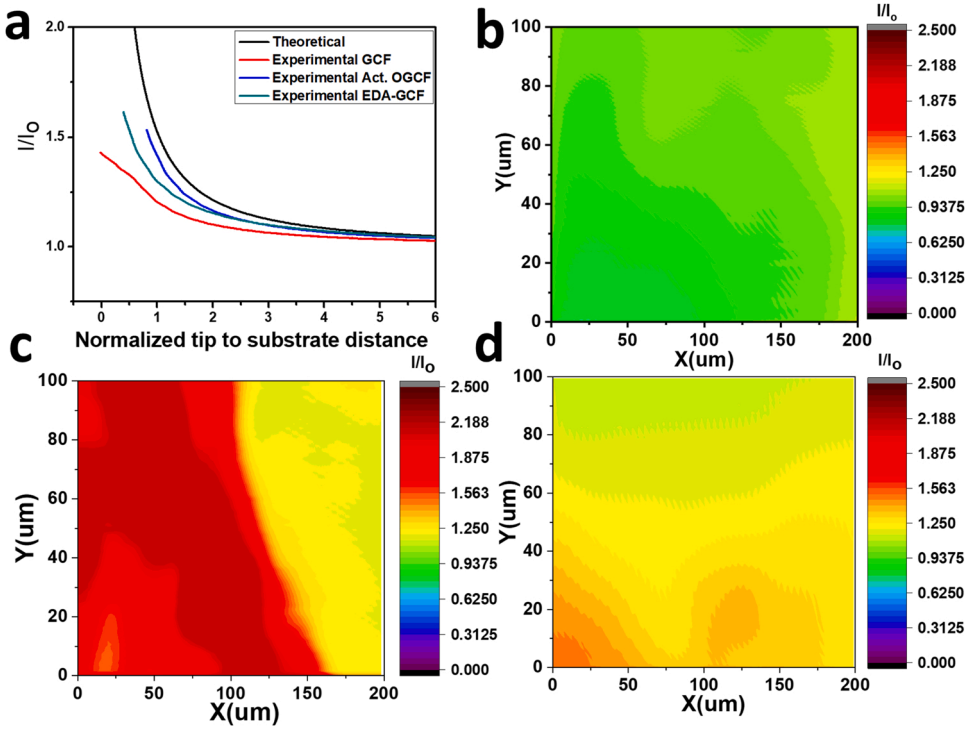

Fig. 6. (a) Approach curves and SECM images recorded above the (b) GCF, (c) Act. OGCF, and (d) EDA-GCF substrates. Redox mediator: 2 mM $[K_4Fe(CN)_6]$; SECM tip, Pt 12.5 μm radius with RG = 8.

the use of an approach curve) [59] and then scanning the tip across the x–y plane parallel with the surface. From the images (Fig. 6b-d), it was evident that, on average, the highest current values were observed at the Act. OGCF and the lowest at GCF. This trend well agrees with the electrochemical CVs and DPVs measurements.

3.2. Characterisation of the immunosensor

Before establishing the performance of the immunosensor for the detection of SARS-CoV-2 SP, the effect of the binding time required to the anti-SARS-CoV-2 to be immobilised onto the EDA-GCF electrode surface, and that required to the SARS-CoV-2 SP to bind to the anti-SARS-CoV-2–modified electrode was investigated and optimized. To this purpose, anti-SARS-CoV-2 (1 μg/mL) was incubated onto the EDA-GCF electrode for 30 min, 1 h, and 3 h in a medium containing PBS (pH 7.4). DPVs, using the $[Fe(CN)_6]^{3-/4-}$ redox couple, were run to establish the inhibition effect on the mass transport resulting from the attachment of anti-SARS-CoV-2 to the EDA-GCF electrode surface. As is shown in Fig. S7, the highest decrease of the current density was obtained after 1 h immobilization. This was therefore considered as the optimized anti-SARS-CoV-2 immobilization time. Then, SARS-CoV-2 SP (1 μg/mL) was allowed to bind at the optimized anti-SARS-CoV-2-modified electrode for 10, 15, 30, and 45 min in PBS (pH 7.4). As is shown in Fig. S8, the highest decrease of the current density occurred when 30 min incubation was employed. The latter was used for the detection of SARS-CoV-2 SP in further electrochemical analyses.

In order to obtain information on surface conductivity/activity upon the attachment of antibody and the SP onto the EDA-GCF surface under the above optimised conditions, SECM images were also recorded (Fig. S9). The attachment of the antibody led to the EDA-GCF surface becoming less conductive/active, compared to bare EDA-GCF, due to the antibody steric hindrance (Fig. S9a), which inhibits the mass transfer of the redox probe towards the active zones of the electrode. The latter effect was further enhanced after the binding of the spike protein to the antibody (Fig. S9b). This result confirmed that the inhibition effect of the mass transport of the $[Fe(CN)_6]^{3-/4-}$ redox couple could be exploited for the SARS-CoV-2 SP quantification.

Fig. 7a shows the DPV responses obtained at EDA-GCF, anti-SARS-CoV-2/EDA-GCF and SARS-CoV-2 SP/anti-SARS-CoV-2/EDA-GCF (prepared in PBS) electrodes, in a solution containing the $[Fe(CN)_6]^{3-/4-}$ redox couple. It is evident that, after the immobilization of the antibody onto the EDA-GCF electrode surface, the J_{pa} decreased from 2.07 mA/cm^2 to 0.93 mA/cm^2, while the anodic peak potential (E_{pa}) shifted from 270 mV to 295 mV, conceivably due to a decrease of the kinetic of the electron transfer process. A similar effect was reported in the literature, upon immobilizing bulky molecules (or other antibodies) onto an electrode surface, and attributed to a steric hindrance, preventing full access of the redox probe to the electrode surface [18,20]. The subsequent binding of the SARS-CoV-2 SP onto the anti-SARS-CoV-2/EDA-GCF, induced an additional decrease of the J_{pa} (down to 0.459 mA/cm^2) and a further positive shift of the E_{pa} (at 321 mV), related to a further steric hindrance due to the SP, which in turn made the electrode surface accessibility more difficult [18,20]. The DPV results are highly consistent with the variation of the J_{pa} and the ΔE_p (0.10, 0.17, and 0.20 V, respectively, for EDA-GCF, anti-SARS-CoV-2/EDA-GCF, and SARS-CoV-2 SP/anti-SARS-CoV-2/EDA-GCF) observed in the CVs (inset of Fig. 7a).

3.2.1. Calibration plots

The effect of SARS-CoV-2 SP concentration on the DPV signals recorded with the immunosensor was investigated. Fig. 7b shows a series of DPVs obtained with the anti-SARS-CoV-2/EDA-GCF sensor, after incubation with SARS-CoV-2 SP at different concentrations (0 −1000 ng/mL in PBS) in a solution containing the $[Fe(CN)_6]^{3-/4-}$ redox probe. The J_{pa} decreased with increasing the SARS-CoV-2 SP concentration and the linear regression analysis of J_{pa} vs. Log[SARS-CoV-2 SP] (inset of Fig. 7b) provided the following equation J_{pa} (μA/cm^2) = − (147 ± 3) log[SARS-CoV-2 SP] (ng/mL) + 468 ± 4(R^2 = 0.998). Error bars refer to the standard deviation obtained from four replicate measurements. The detection limit, obtained as the signal to noise ratio equal to three (S/N = 3), was 27 pg/mL.

The performance of the immunosensor for the detection of SARS-

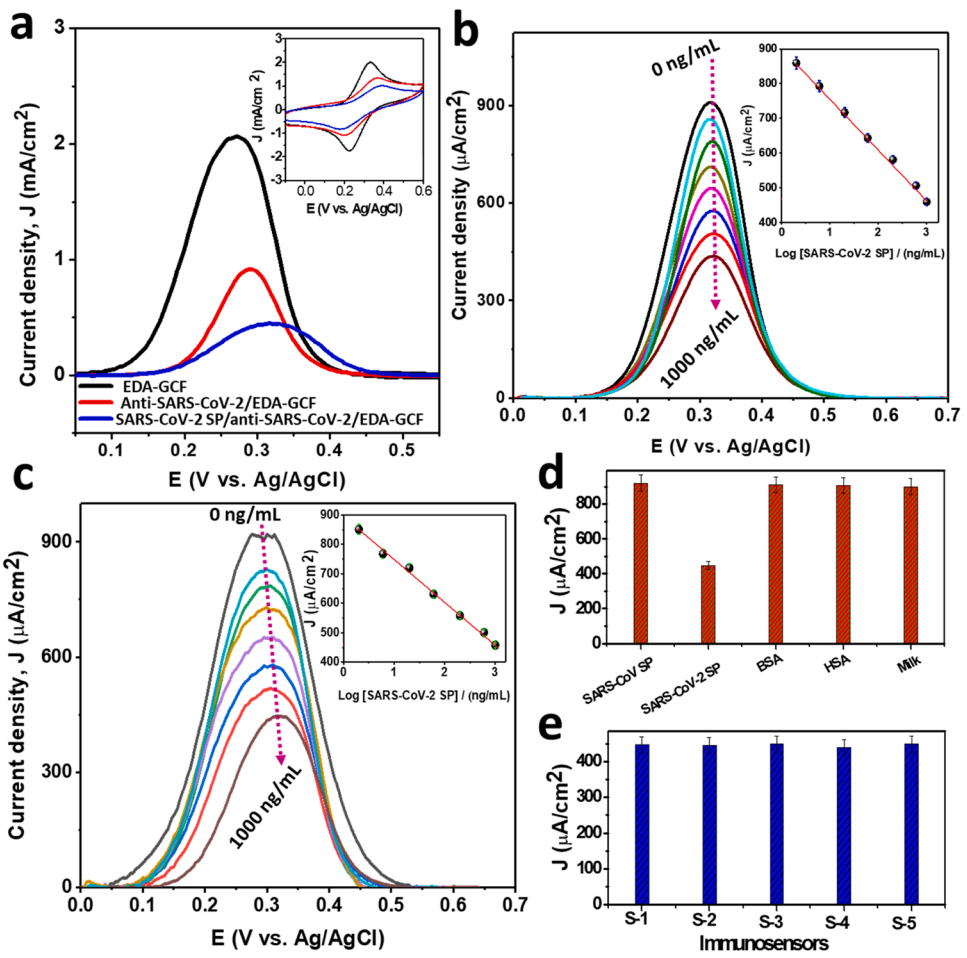

Fig. 7. DPV responses of EDA-GCF, anti-SARS-CoV-2/EDA-GCF, and SARS-CoV-2 SP anti-SARS-CoV-2/EDA-GCF electrodes in $[Fe(CN)_6]^{3-/4-}$ solution (inset shows the corresponding CV responses at a scan rate of 100 mV/s). (b) DPV responses of the anti-SARS-CoV-2/EDA-GCF sensor probe with the binding of different concentrations of SARS-CoV-2 SP (0, 2, 6, 20, 60, 200, 600, and 1000 ng/mL in PBS. (c) DPV responses of the anti-SARS-CoV-2/EDA-GCF sensor probe with the binding of different concentrations of SARS-CoV-2 SP (0, 2, 6, 20, 60, 200, 600, and 1000 ng/mL in diluted BP) (inset shows the corresponding calibration plot). (d) Bar diagram of the DPV current responses upon the binding of SARS-CoV-2 SP and different interferences and (e) DPV current responses of five different immunosensors upon the binding of SARS-CoV-2 SP. Insets in Fig. b,c show the calibration plots obtained using the DPV peak current as a function of the logarithm of concentration of SARS-CoV-2 SP; the error bars refer to the standard deviation evaluated from four replicate measurements.

CoV-2 SP was also examined in diluted human BP samples, to ascertain whether endogenous compounds present in body fluids could affect the DPV signals. BP was diluted with PBS and subsequently spiked with varying concentrations of SARS-CoV-2 SP. Fig. 7c shows the DPV signals recorded for $[Fe(CN)_6]^{3-/4-}$ at the anti-SARS-CoV-2/EDA-GCF by changing the SARS-CoV-2 SP concentration over the range 0–1000 ng/mL, while the inset of Fig. 7c displays the relevant calibration plot. The linear regression analysis of the experimental points provided: J_{pa} (μA/cm^2) = − (144 ± 4 log[SARS-CoV-2 SP] (μg/mL) + 462 ± 5 (R^2 = 0.998) and LOD (S/N = 3) of 25 pg/mL. The values of intercept and slope, obtained in diluted BP, were very close to those evaluated in PBS, suggesting that the proposed sensor is suitable for practical detection of SARS-CoV-2 SP in real biological samples.

To further support the latter claim, the immunosensor was employed to detect SARS-CoV-2 SP in diluted (100 times with PBS, pH 7.4) artificial human saliva. In fact, it is reported that 84.6–91.7% of COVID-19-affected patients carry a detectable viral load of SARS-CoV-2 virus in saliva [60,61]. Two saliva samples spiked with 300 ng/mL and 500 ng/mL of SARS-CoV-2 SP were examined by DPV, following the same procedure described above. It is interesting to note that the baseline of DPV responses, due to the $[Fe(CN)_6]^{3-/4-}$ redox couple, in the latter samples without SARS-CoV-2 SP overlapped those recorded in both diluted BP and PBS samples with no protein. This indicated that saliva components did not cause substantial interference in the detection process, which also agrees with recent literature reports [62]. The concentration of SARS-CoV-2 SP in the saliva samples was quantified using the calibration plot in Fig. 7c (inset), and the recovery values found, ranging from 98.0% to 104.0%, are shown in Table S2. These results further confirm the practicability of the immunosensor proposed here for diagnosing COVID-19, at least, for first-line screening tests in several environments.

3.2.2. *Selectivity, reproducibility, stability, and repeatability study*

The selectivity of the immunosensor was evaluated by comparing the DPVs for the $[Fe(CN)_6]^{3-/4-}$ redox probe obtained with the anti-SARS-CoV-2/EDA-GCF sensor using SARS-CoV SP (5 μg/mL), SARS-CoV-2 SP (1 μg/mL), BSA (5 μg/mL), HSA (5 μg/mL), and different available proteins from diluted milk. The corresponding DPV responses are summarized in Fig. 7d. No significant current change was induced by the SARS-CoV SP, BSA, HSA, and proteins from milk, indicating that the immunosensor is highly specific to SARS-CoV-2 SP.

The reproducibility of the anti-SARS-CoV-2/EDA-GCF probe preparation was investigated using five independent immunosensors. The corresponding DPV results (Fig. 7e), obtained after incubation of the sensors with SARS-CoV-2 SP (1 μg/mL in PBS), revealed a very low RSD (1.2%) for the J_{pa} of $[Fe(CN)_6]^{3-/4-}$ signals, suggesting the high reproducibility in the preparation of the immunosensors.

Electrochemical stability of the immunosensor was investigated by performing seven consecutive DPVs (Fig. 8a) and a CA (Fig. S10) for 1 h. The DPV results revealed a very low RSD (1.90%) for the J_{pa} of the $[Fe(CN)_6]^{4-}$ oxidation process, while the current density of the CA response remained almost unchanged after 1 h. These results indicated the high electrochemical stability of the immunosensor and its suitability for a series of point-of-care measurements.

The repeatability of the immunosensor was studied after storing the sensor for three weeks at 4 °C. The J_{pa} for the $[Fe(CN)_6]^{4-}$ oxidation process, obtained from the DPV responses, recorded after incubation of the sensor with SARS-CoV-2 SP (1 μg/mL in PBS), measured at one-week

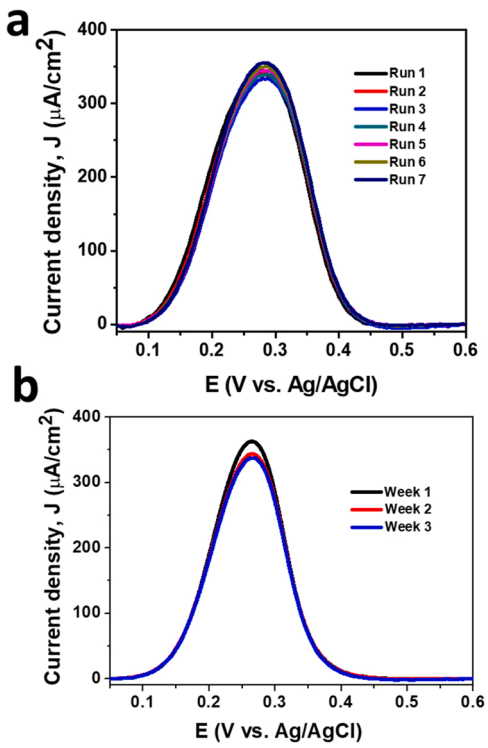

Fig. 8. (a) Repetitive DPVs recorded at a freshly prepared immunosensor and (b) after storing the sensor for three weeks at 4 °C (measured every week interval) for the oxidation of $[Fe(CN)6]^{3-/4-}$ after the binding of SARS-CoV-2 SP (1 μg/mL) in PBS (pH 7.4).

intervals, revealed a very low RSD (3.3%) (Fig. 8b). These results also confirm that the proposed immunosensor is highly suitable for the development of accurate and reliable disposable SARS-CoV-2 detection systems.

Finally, the general analytical performance of the immunosensor developed here resulted much better or comparable with those reported in the literature, in which other types of immunosensors for the detection of SARS-CoV-2 SP were employed, as summarized in Table S3. In addition, sensitivity and LOD, in terms of antigen concentration, are well lower than those reported in the literature using commercial SARS-CoV-2 rapid point-of-care antigen tests [63,64] (i.e., about a few ng/mL), whose clinical performance was compared with SARS-CoV-2 viral loads obtained using the reference method of RT-rtPCR [63].

4. Conclusions

In summary, a self-supported EDA functionalized GCF electrode was developed for the label-free detection of SARS-CoV-2 SP. This was constructed by the controlled and partial oxidation and exfoliation of the GCF surface and a consequent EDA functionalization. The EDA-GCF electrode served as the anti-SARS-CoV-2 immobilization matrix, at whose surface SARS-CoV-2 SP could bind, thus allowing its label-free quantification, using the $[Fe(CN)_6]^{3-/4-}$ redox couple. The immunosensor thus prepared could detect SARS-CoV-2 SP in PBS, diluted blood plasma and artificial human saliva samples over a wide concentration range, with an average LOD of 26 pg/mL, without any significant interference from other proteins, such as BSA, HSA and those present in the SARS-CoV virus.

The self-supported electrode proposed here could be advantageous for developing sensors with high sensitivity, stability, and low cost. Furthermore, the flexibility of the anti-SARS-CoV-2-modified EDA-GCF electrode is promising to prepare wearable sensing devices to be integrated, for instance, in face masks, and along with suitable electronics can be used for remote monitoring patients affected by COVID-19 disease. In addition, the measurements can be performed with portable instruments, which are of crucial importance to POC and wearable detection apparatuses. From a practical perspective, knowledge of the analytical sensitivity rather than clinical sensitivity using sensors as those described here, might be sufficient to judge their utility in various fields of application (e.g., screening in outpatient departments and testing in the workplace or the general population), as compared with the well-established reference method of RT-PCR [54,63].

Finally, the work presented here could open a new avenue for developing flexible and self-supported electrodes for various electroanalytical applications using other low-cost carbon-based electrodes (e.g., carbon cloth, carbon fiber sheet, etc.).

Compliance with ethical standards

The author(s) declare that they have no competing interests.

CRediT authorship contribution statement

M.Adeel: Conceptualization of experimental ideas, first writing original draft, experimental operation, data processing analysis; K. Asif: Experimental operation and support in data analysis; V. Canzonieri: Revise the draft; H. R. Barai: Experimental operation; Md. M. Rahman: implementation of experiments, discuss the experimental data and revise the manuscript; S. Daniele: supervise the study, co-write original draft of the manuscript and revise the final version; F. Rizzolio: experimental supervision, and writing guidance, discuss the experimental data.

Declaration of Competing Interest

The authors declare that they have no known competing financial interests or personal relationships that could have appeared to influence the work reported in this paper.

Acknowledgment

This work was with the COST Action STRATAGEM CA17104, supported by COST (European Cooperation in Science and Technology) (www.cost.eu), and also within the program SPIN-Supporting Principal Investigators, Ca' Foscari University Venice, Italy, N° 9L2AC3B8.

Appendix A. Supporting information

Supplementary data associated with this article can be found in the online version at doi:10.1016/j.snb.2022.131591.

References

[1] C. Wang, P.W. Horby, F.G. Hayden, G.F. Gao, A novel coronavirus outbreak of global health concern, Lancet 395 (2020) 470–473, https://doi.org/10.1016/S0140-6736(20)30185-9.
[2] M.E.S. El Keshky, S.S. Basyouni, A.M.Al Sabban, Getting through COVID-19: the pandemic's impact on the psychology of sustainability, quality of life, and the global economy – a systematic review, Front. Psychol. 11 (2020) 5858769, https://doi.org/10.3389/fpsyg.2020.585897.
[3] J. Lukose, S. Chidangil, S.D. George, Optical technologies for the detection of viruses like COVID-19: Progress and prospects, Biosens. Bioelectron. 178 (2021), 113004, https://doi.org/10.1016/j.bios.2021.113004.
[4] H. Zhao, F. Liu, W. Xie, T.C. Zhou, J. OuYang, L. Jin, H. Li, C.Y. Zhao, L. Zhang, J. Wei, Y.P. Zhang, C.P. Li, Ultrasensitive supersandwich-type electrochemical sensor for SARS-CoV-2 from the infected COVID-19 patients using a smartphone, Sens. Actuators, B Chem. 327 (2021), 128899, https://doi.org/10.1016/j.snb.2020.128899.
[5] A. Raziq, A. Kidakova, R. Boroznjak, J. Reut, A. Öpik, V. Syritski, Development of a portable MIP-based electrochemical sensor for detection of SARS-CoV-2 antigen, Biosens. Bioelectron. 178 (2021), 113029, https://doi.org/10.1016/j.bios.2021.113029.

[6] C.R. Dennison Himmelfarb, D. Baptiste, Coronavirus disease (COVID-19) implications for cardiovascular and socially at-risk populations, J. Cardiovasc. Nurs. 35 (2020) 318–321, https://doi.org/10.1097/jcn.0000000000000710.

[7] C.C. Lai, C.Y. Wang, W.C. Ko, P.R. Hsueh, In vitro diagnostics of coronavirus disease 2019: technologies and application, J. Microbiol. Immunol. Infect. 54 (2020) 164–174, https://doi.org/10.1016/j.jmii.2020.05.016.

[8] N. Taleghani, F. Taghipour, Diagnosis of COVID-19 for controlling the pandemic: a review of the state-of-the-art, Biosens. Bioelectron. 174 (2021), 112830, https://doi.org/10.1016/j.bios.2020.112830.

[9] M. Yüce, E. Filiztekin, K.G. Özkaya, COVID-19 diagnosis —a review of current methods, Biosens. Bioelectron. 172 (2021), 112752, https://doi.org/10.1016/j.bios.2020.112752.

[10] A. Hachim, N. Kavian, C.A. Cohen, A.W.H. Chin, D.K.W. Chu, C.K.P. Mok, O.T. Y. Tsang, Y.C. Yeung, R.A.P.M. Perera, L.L.M. Poon, J.S.M. Peiris, S.A. Valkenburg, ORF8 and ORF3b antibodies are accurate serological markers of early and late SARS-CoV-2 infection, Nat. Immunol. 21 (2020) 1293–1301, https://doi.org/10.1038/s41590-020-0773-7.

[11] P. Diamandis, I. Prassas, E.P. Diamandis, E.P. Diamandis, E.P. Diamandis, E. P. Diamandis, Antibody tests for COVID-19: drawing attention to the importance of analytical specificity, Clin. Chem. Lab. Med. 58 (2020) 1144–1145, https://doi.org/10.1515/cclm-2020-0554.

[12] W. Zhang, R.H. Du, B. Li, X.S. Zheng, X. Lou Yang, B. Hu, Y.Y. Wang, G.F. Xiao, B. Yan, Z.L. Shi, P. Zhou, Molecular and serological investigation of 2019-nCoV infected patients: implication of multiple shedding routes, Emerg. Microbes Infect. 9 (2020) 386–389, https://doi.org/10.1080/22221751.2020.1729071.

[13] L. Ying, L. Yue-Ping, D. Bo, R. Feifei, W. Yue, D. Jinya, H. Qianchuan, Diagnostic indexes of a rapid IgG/IgM combined antibody test for SARS-CoV-2, MedRxiv (2020), https://doi.org/10.1101/2020.03.26.20044883.

[14] Coronavirus Disease 2019 (COVID-19) Emergency Use Authorizations for Medical Devices | FDA, 2020. ⟨https://www.fda.gov/medical-devices/emergency-use-authorizations-medical-devices/coronavirus-disease-2019-covid-19-emergency-use-authorizations-medical-devices⟩.

[15] T. Stanborough, F.M. Given, B. Koch, C.R. Sheen, A.B. Stowers-Hull, M. R. Waterland, D.L. Crittenden, Optical detection of CoV-SARS-2 viral proteins to sub-picomolar concentrations, ACS Omega 6 (2021) 6404–6413, https://doi.org/10.1021/acsomega.1c00008.

[16] G. Seo, G. Lee, M.J. Kim, S.H. Baek, M. Choi, K.B. Ku, C.S. Lee, S. Jun, D. Park, H. G. Kim, S.J. Kim, J.O. Lee, B.T. Kim, E.C. Park, S. Il Kim, Rapid detection of COVID-19 causative virus (SARS-CoV-2) in human nasopharyngeal swab specimens using field-effect transistor-based biosensor, ACS Nano 14 (2020) 5135–5142, https://doi.org/10.1021/acsnano.0c02823.

[17] W. Shao, M.R. Shurin, S.E. Wheeler, X. He, A. Star, Rapid detection of SARS-CoV-2 antigens using high-purity semiconducting single-walled carbon nanotube-based field-effect transistors, ACS Appl. Mater. Interfaces 13 (2021) 10321–10327, https://doi.org/10.1021/acsami.0c22589.

[18] B. Mojsoska, S. Larsen, D.A. Olsen, J.S. Madsen, I. Brandslund, F.A. Alatraktchi, Rapid SARS-CoV-2 detection using electrochemical immunosensor, Sensors 21 (2021) 1–11, https://doi.org/10.3390/s21020390.

[19] S. Mahari, A. Roberts, D. Shahdeo, S. Gandhi, Ecovsens-ultrasensitive novel in-house built printed circuit board based electrochemical device for rapid detection of nCovid-19 antigen, a spike protein domain 1 of SARS-CoV-2, BioRxiv (2020), https://doi.org/10.1101/2020.04.24.059204.

[20] Z. Rahmati, M. Roushani, H. Hosseini, H. Choobin, Electrochemical immunosensor with Cu2O nanocube coating for detection of SARS-CoV-2 spike protein, Microchim. Acta 188 (2021) 105, https://doi.org/10.1007/s00604-021-04762-9.

[21] M. Adeel, M.M. Rahman, I. Caligiuri, V. Canzonieri, F. Rizzolio, S. Daniele, Recent advances of electrochemical and optical enzyme-free glucose sensors operating at physiological conditions, Biosens. Bioelectron. 165 (2020), 112321, https://doi.org/10.1016/J.BIOS.2020.112331.

[22] M. Adeel, V. Canzonieri, S. Daniele, A. Vomiero, F. Rizzolio, M.M. Rahman, 2D metal azolate framework as nanozyme for amperometric detection of glucose at physiological pH and alkaline medium, Microchim. Acta 188 (2021) 77, https://doi.org/10.1007/S00604-021-04737-W.

[23] S.A. Lim, M.U. Ahmed, Electrochemical immunosensors and their recent nanomaterial-based signal amplification strategies: A review, RSC Adv. 6 (2016) 24995–25014, https://doi.org/10.1039/c6ra00333h.

[24] M. Adeel, V. Canzonieri, S. Daniele, F. Rizzolio, M.M. Rahman, Organobase assisted synthesis of Co(OH)2 nanosheets enriched with oxygen vacancies for nonenzymatic glucose sensing at physiological pH, J. Ind. Eng. Chem. 103 (2021) 165–174, https://doi.org/10.1016/j.jiec.2021.07.030.

[25] N.S. Lopa, M.M. Rahman, F. Ahmed, T. Ryu, S.C. Sutradhar, J. Lei, J. Kim, D. H. Kim, Y.H. Lee, W. Kim, Simple, low-cost, sensitive and label-free aptasensor for the detection of cardiac troponin I based on a gold nanoparticles modified titanium foil, Biosens. Bioelectron. 126 (2019) 381–388, https://doi.org/10.1016/j.bios.2018.11.012.

[26] M. Adeel, M.M. Rahman, J.J. Lee, Label-free aptasensor for the detection of cardiac biomarker myoglobin based on gold nanoparticles decorated boron nitride nanosheets, Biosens. Bioelectron. 126 (2019) 143–150, https://doi.org/10.1016/j.bios.2018.10.060.

[27] M. Adeel, K. Asif, M.M. Rahman, S. Daniele, V. Canzonieri, F. Rizzolio, Glucose detection devices and methods based on metal–organic frameworks and related materials, Adv. Funct. Mater. 31 (2021) 2106023, https://doi.org/10.1002/adfm.202106023.

[28] O. Fernando, E. Magner, Biosensors—recent advances and future challenges in electrode materials, Sensors 20 (2020) 1–17, https://doi.org/10.3390/s20123561.

[29] R. Kour, S. Arya, S.-J. Young, V. Gupta, P. Bandhoria, A. Khosla, Review—recent advances in carbon nanomaterials as electrochemical biosensors, J. Electrochem. Soc. 167 (2020), 037555, https://doi.org/10.1149/1945-7111/ab6bc4.

[30] M.E. Khan, State-of-the-art developments in carbon-based metal nanocomposites as a catalyst: photocatalysis, Nanoscale Adv. 3 (2021) 1887–1900, https://doi.org/10.1039/d1na00041a.

[31] J. Zhang, Z. Xia, L. Dai, Carbon-based electrocatalysts for advanced energy conversion and storage, Sci. Adv. 1 (2015), https://doi.org/10.1126/sciadv.1500564.

[32] M.M. Rahman, N.S. Lopa, M.J. Ju, J.J. Lee, Highly sensitive and simultaneous detection of dopamine and uric acid at graphene nanoplatelet-modified fluorine-doped tin oxide electrode in the presence of ascorbic acid, J. Electroanal. Chem. 792 (2017) 54–60, https://doi.org/10.1016/j.jelechem.2017.03.038.

[33] J.H. Shin, M.J. Lee, J.H. Choi, J. ae Song, T.H. Kim, B.K. Oh, Electrochemical H2O2 biosensor based on horseradish peroxidase encapsulated protein nanoparticles with reduced graphene oxide-modified gold electrode, Nano Converg. 7 (2020), https://doi.org/10.1186/s40580-020-00249-0.

[34] A. Navaee, A. Salimi, H. Teymourian, Graphene nanosheets modified glassy carbon electrode for simultaneous detection of heroine, morphine and noscapine, Biosens. Bioelectron. 31 (2012) 205–211, https://doi.org/10.1016/j.bios.2011.10.018.

[35] Y. Wang, B. Song, J. Xu, S. Hu, An amperometric sensor for nitric oxide based on a glassy carbon electrode modified with graphene, Nafion, and electrodeposited gold nanoparticles, Microchim. Acta 182 (2015) 711–718, https://doi.org/10.1007/s00604-014-1379-2.

[36] D. Kim, S. Lee, Y. Piao, Electrochemical determination of dopamine and acetaminophen using activated graphene-Nafion modified glassy carbon electrode, J. Electroanal. Chem. 794 (2017) 221–228, https://doi.org/10.1016/j.jelechem.2017.04.018.

[37] W. Choi, I. Lahiri, R. Seelaboyina, Y.S. Kang, Synthesis of graphene and its applications: a review, Crit. Rev. Solid State Mater. Sci. 35 (2010) 52–71, https://doi.org/10.1080/10408430903505036.

[38] I. Ciani, P.D. Burt, S. Daniele, P.R. Unwin, Effect of surface pressure on oxygen transfer across molecular monolayers at the air/water interface: scanning electrochemical microscopy investigations using a mercury hemispherical microelectrode probe, J. Phys. Chem. B 108 (2004) 3801–3809, https://doi.org/10.1021/jp036286m.

[39] Y. saito, A theoretical study on the diffusion current at the stationary electrodes of circular and narrow band types, Rev. Polarogr. 15 (1968) 177–187, https://doi.org/10.5189/revpolarography.15.177.

[40] D. Battistel, G. Pecchielan, S. Daniele, Micropipette contact technique as a tool to reveal, characterize, and modify nanopore electrodes, ChemElectroChem 1 (2014), https://doi.org/10.1002/celc.201300147.

[41] J.L. Amphlett, G. Denuault, Scanning Electrochemical Microscopy (SECM): an investigation of the effects of tip geometry on amperometric tip response, J. Phys. Chem. B 102 (1998) 9946–9951, https://doi.org/10.1021/jp982829u.

[42] G. Lindsey, S. Abercrombie, G. Denuault, S. Daniele, E.D. Faveri, Scanning electrochemical microscopy: Approach curves for sphere-cap scanning electrochemical microscopy tips, Anal. Chem. 79 (2007) 2952–2956, https://doi.org/10.1021/ac061427c.

[43] M.C. Hsiao, S.H. Liao, M.Y. Yen, P.I. Liu, N.W. Pu, C.A. Wang, C.C.M. Ma, Preparation of covalently functionalized graphene using residual oxygen-containing functional groups, ACS Appl. Mater. Interfaces 2 (2010) 3092–3099, https://doi.org/10.1021/am100597d.

[44] J. Pei, T. Zhang, H. Suo, Graphene preparation and process parameters by pre-intercalation assisted electrochemical exfoliation of graphite, J. Solid State Electrochem. 25 (2021) 1245–1257, https://doi.org/10.1007/s10008-021-04899-w.

[45] W. Wan, F. Zhang, S. Yu, R. Zhang, Y. Zhou, Hydrothermal formation of graphene aerogel for oil sorption: the role of reducing agent, reaction time and temperature, N. J. Chem. 40 (2016) 3040–3046, https://doi.org/10.1039/c5nj03086b.

[46] L. Wang, Y. Park, P. Cui, S. Bak, H. Lee, S.M. Lee, H. Lee, Facile preparation of an n-type reduced graphene oxide field effect transistor at room temperature, Chem. Commun. 50 (2014) 1224–1226, https://doi.org/10.1039/c3cc47224h.

[47] W. Zhang, M.M. Rahman, F. Ahmed, N.S. Lopa, C. Ge, T. Ryu, S. Yoon, L. Jin, H. Jang, W. Kim, A two-step approach for improved exfoliation and cutting of boron nitride into boron nitride nanodisks with covalent functionalizations, Nanotechnology 31 (2020), https://doi.org/10.1088/1361-6528/ab9a76.

[48] F. Samadaei, M. Salami-Kalajahi, H. Roghani-Mamaqani, M. Banaei, A structural study on ethylenediamine- and poly(amidoamine)-functionalized graphene oxide: simultaneous reduction, functionalization, and formation of 3D structure, RSC Adv. 5 (2015) 71835–71843, https://doi.org/10.1039/c5ra12086a.

[49] W. Li, D. Li, Q. Fu, C. Pan, Conductive enhancement of copper/graphene composites based on high-quality graphene, RSC Adv. 5 (2015) 80428–80433, https://doi.org/10.1039/c5ra15189a.

[50] Y. Shao, S. Zhang, C. Wang, Z. Nie, J. Liu, Y. Wang, Y. Lin, Highly durable graphene nanoplatelets supported Pt nanocatalysts for oxygen reduction, J. Power Sources 195 (2010) 4600–4605, https://doi.org/10.1016/j.jpowsour.2010.02.044.

[51] K. Kordek, L. Jiang, K. Fan, Z. Zhu, L. Xu, M. Al-Mamun, Y. Dou, S. Chen, P. Liu, H. Yin, P. Rutkowski, H. Zhao, Two-step activated carbon cloth with oxygen-rich functional groups as a high-performance additive-free air electrode for flexible zinc–air batteries, Adv. Energy Mater. 9 (2019) 1802936, https://doi.org/10.1002/aenm.201802936.

[52] J. Nimita Jebaranjitham, C. Mageshwari, R. Saravanan, N. Mu, Fabrication of amine functionalized graphene oxide – AgNPs nanocomposite with improved dispersibility for reduction of 4-nitrophenol, Compos. Part B Eng. 171 (2019) 302–309, https://doi.org/10.1016/j.compositesb.2019.05.018.

[53] Y. Ding, F. Zhang, J. Xu, Y. Miao, Y. Yang, X. Liu, B. Xu, Synthesis of short-chain passivated carbon quantum dots as the light emitting layer towards electroluminescence, RSC Adv. 7 (2017) 28754–28762, https://doi.org/10.1039/c7ra02421e.
[54] S. Ravi, S. Zhang, Y.R. Lee, K.K. Kang, J.M. Kim, J.W. Ahn, W.S. Ahn, EDTA-functionalized KCC-1 and KIT-6 mesoporous silicas for Nd3+ ion recovery from aqueous solutions, J. Ind. Eng. Chem. 67 (2018) 210–218, https://doi.org/10.1016/j.jiec.2018.06.031.
[55] M. Mahbubur Rahman, J.J. Lee, Sensitivity control of dopamine detection by conducting poly(thionine), Electrochem. Commun. 125 (2021), 107005, https://doi.org/10.1016/j.elecom.2021.107005.
[56] M. Rohani Moghadam, L. Salehi, S. Jafari, N. Nasirizadeh, J. Ghasemi, Voltammetric sensing of oxacillin by using a screen-printed electrode modified with molecularly imprinted polyaniline, gold nanourchins and graphene oxide, Microchim. Acta 186 (2019) 798, https://doi.org/10.1007/s00604-019-3981-9.
[57] S.R. Chinnadayyala, S. Cho, Electrochemical immunosensor for the early detection of rheumatoid arthritis biomarker: Anti-cyclic citrullinated peptide antibody in human serum based on avidin-biotin system, Sensors 21 (2021) 1–16, https://doi.org/10.3390/s21010124.
[58] H.R. Barai, N.S. Lopa, F. Ahmed, N.A. Khan, S.A. Ansari, S.W. Joo, M.M. Rahman, Synthesis of Cu-doped Mn3O4@Mn-doped CuO nanostructured electrode materials by a solution process for high-performance electrochemical pseudocapacitors, ACS Omega 5 (2020) 22356–22366, https://doi.org/10.1021/acsomega.0c02740.
[59] A.J. Bard, M.V. Mirkin, Scanning electrochemical microscopy (2012) 670 https://doi.org/10.1201/b11850.
[60] K.K.W. To, O.T.Y. Tsang, C.C.Y. Yip, K.H. Chan, T.C. Wu, J.M.C. Chan, W.S. Leung, T.S.H. Chik, C.Y.C. Choi, D.H. Kandamby, D.C. Lung, A.R. Tam, R.W.S. Poon, A.Y. F. Fung, I.F.N. Hung, V.C.C. Cheng, J.F.W. Chan, K.Y. Yuen, Consistent detection of 2019 novel coronavirus in saliva, Clin. Infect. Dis. 71 (2020) 841–843, https://doi.org/10.1093/cid/ciaa149.
[61] E. Williams, K. Bond, B. Zhang, M. Putland, D.A. Williamson, Saliva as a noninvasive specimen for detection of sars-cov-2, J. Clin. Microbiol. 58 (2020), https://doi.org/10.1128/JCM.00776-20.
[62] A. Ramanujam, S. Almodovar, G.G. Botte, Ultra-fast electrochemical sensor for point-of-care covid-19 diagnosis using non-invasive saliva sampling, Processes 9 (2021) 1236, https://doi.org/10.3390/pr9071236.
[63] V.M. Corman, V.C. Haage, T. Bleicker, M.L. Schmidt, B. Mühlemann, M. Zuchowski, W.K. Jo, P. Tscheak, E. Möncke-Buchner, M.A. Müller, A. Krumbholz, J.F. Drexler, C. Drosten, Comparison of seven commercial SARS-CoV-2 rapid point-of-care antigen tests: a single-centre laboratory evaluation study, Lancet 2 (2021), e311, https://doi.org/10.1016/S2666-5247(21)00056-2.
[64] M. Di Domenico, A. De Rosa, M. Boccellino, Detection of SARS-COV-2 proteins using an ELISA test, Diagnostics 11 (2021) 698, https://doi.org/10.3390/diagnostics11040698.

Muhammed Adeel has just received his PhD in Science and Technology of Bio and Nanomaterials at the University Cà Foscari of Venice (Italy) (January 2022). He is now post-doc at the Department of Molecular sciences and Nanosystems of the University Cà Foscari of Venice (Italy). His current research activity focuses on the development of novel materials for electrochemical sensors and their application for electroanalysis in synthetic and real samples and in cancer therapy.

Kanwal Asif is a second year Ph.D student with Prof Flavio Rizzolio, and Prof Vincenzo Canzonieri in Science and Technology of Bio and Nanomaterials at the University Cà Foscari of Venice (Italy). Her current research activity focuses on the use self-therapeutic nanomaterials for cancer treatments.

Vincenzo Canzonieri is currently associate professor of pathology at the University of Trieste and Director of the Pathology Department at the Aviano Cancer Center CRO, NCI. He attended the Residency in Anatomic Pathology at the University of Padova, the Residency in General Oncology at the University of Catania and the residency in Forensic Medicine at the University of Udine. He obtained also a mini MBA in sanitary management at the University Bocconi in Milan in 2010. His research activities focus on digital pathology and morphological, phenotypic and genotypic characterizations of GYN, GI, soft tissue tumors and lymphomas.

Hasi Rani Barai is assistant professor in the School of Mechanical and IT Engineering, Yeungnam University, Korea. She worked as a postdoctoral research fellow in the Department of Chemistry and Nanoscience, Ewha Woman's University, Korea, and the Department of Chemistry, Sogang University, Korea. She received her Ph.D. in the Department of Chemistry and Chemical Engineering, Inha University, Korea, and MS degree in Dhaka University, Bangladesh. Her research interest interests include the development of nanomaterials for supercapacitors applications.

Md. Mahbubur Rahman is associate professor at Konkuk University, since September 2021. He received the M.S. degree in Chemistry in 2005 from the University of Dhaka, Bangladesh, and a Ph.D. degree in electrochemistry in 2014 from Konkuk University, Korea. He also worked as a postdoctoral scholar at Incheon National University, Korea. His research interests include the development of nanomaterials for various electrochemical and photo-electrochemical technologies.

Salvatore Daniele is full professor of analytical chemistry at the Department of Molecular Science and Nanosystems at the University Cà Foscari Venice (Italy). He is member of the International Society of Electrochemsitry (ISE), and in the paste was appointed as Chair of the Division 1 (Analytical Electrochemistry). His research activity focuses on the development of electrochemical sensors for electroanalysis in synthetic and real samples, including food and biologic fluids, and on investigation of electrode processes using micro/nanoelectrodes and scanning electrochemical microscopy.

Flavio Rizzolio is full professor in Molecular Biology at the Department of Molecular Science and Nanosystems at the University Cà Foscari of Venice (Italy). His work started by studying the genetic alterations causative of ovarian dysfunctions, followed by a second phase dedicated to the mechanisms of cell cycle control in cancer and finally, a nanomedicine approach for cancer therapy.